Pre-equilibrium emission effects in the measured isomeric yield ratios in alpha-induced reactions on ^{197}Au

N. Chakravarty

Radiochemistry Division, Bhabha Atomic Research Centre, Bombay 400085, India

P. K. Sarkar

Health Physics Unit, Variable Energy Cyclotron Centre, I/AF Bidhan Nagar, Calcutta 700064, India

Sudip Ghosh

Saha Institute of Nuclear Physics, I/AF Bidhan Nagar, Calcutta 700064, India

Excitation functions of isomeric yields have been measured for ^{198}Tl, ^{197}Hg, ^{198}Au, and ^{196}Au produced by $\alpha + ^{197}$Au reactions in the 35–50 MeV energy range. The isomeric yield ratios are analyzed in terms of pre-equilibrium and evaporation emissions. Single as well as two-nucleon pre-equilibrium emissions are taken into account. Various combinations of pre-equilibrium and equilibrium emissions together with different sequences in which the ejectiles may be emitted are explicitly considered to evaluate the average spin distribution of the final nucleus. The choice of the spin cutoff parameter and the effect of forward-angle emissions of pre-equilibrium particles have been investigated. The isomeric yield ratios are found to depend sensitively on the pre-equilibrium angular distribution and on the spin cutoff parameter for equilibrium emissions. Inadequate description of the reaction mechanism leads to incorrect predictions of excitation functions as well as isomeric yield ratios.

PACS number(s): 25.55.−e, 25.90.+k

I. INTRODUCTION

In a nuclear reaction resulting in the formation of a nucleus with a low-lying isomeric state, the relative population of the isomeric state with respect to the ground state is governed by the spin distribution of the residual nucleus [1,2]. This spin distribution is determined by the angular momentum brought in by the projectile and that carried away by the ejectiles. The former depends on the projectile and its energy. The loss of angular momentum during particle emissions depends on the number and type of ejectiles as well as on the emission mechanism—a pre-equilibrium (PEQ) emission will result in a larger angular momentum being carried away than in the case of an equilibrium (EQ) compound nuclear emission. Again, the PEQ component of the reaction cross section increases with projectile energy. Thus the study of the isomeric cross-section ratios (IR's) for the nuclei formed from the same target-projectile combination at different projectile energies is of fundamental interest in understanding the role of the reaction mechanism in determining the spin distribution of the residual nucleus. Measured values of IR's have been used to study the level density and discrete level structures of nuclei [3,4]. Variations of IR's with incident energy have been analyzed in the framework of compound-nucleus theory [5–7]. Attempts have also been made to explain IR's for reactions with significant PEQ emissions [4,7–10].

The earlier of these studies [4,8–10] of IR's in terms of PEQ emissions were mostly concerned with nuclei formed through neutron emissions. Recently, Nagame *et al.* [7] have measured and analyzed IR's of nuclei formed through charged-particle emissions. In their theoretical analysis, however, they do not take into account the depletion of angular momentum resulting from PEQ emission. They assume the spin distribution of the composite nucleus for the nucleus formed after PEQ emission of a proton or neutron.

In this paper we report the measured IR's for ^{198}Tl, ^{197}Hg, ^{198}Au, and ^{196}Au formed through alpha-induced reactions on ^{197}Au at incident energies of 35–50 MeV. The IR's for ^{197}Hg, ^{198}Au, and ^{196}Au for $\alpha + ^{197}$Au reactions involving charged-particle emissions have not been reported earlier in this energy range. Cross sections for ^{197}Au$(\alpha,3n)$ ^{198}Tl and the corresponding IR's, have been published earlier over a wide energy range [11–13], but previous cross-section measurements of ^{197}Hg through alpha irradiation of ^{197}Au was confined only to the metastable state (0.299 MeV, $\frac{13}{2}^+$). This is because ^{197}Hg is a nonshielded nucleus in the sense that the ground state of ^{197}Hg is formed through the ^{197}Au$(\alpha,p3n)^{197}$Hg as well as through 100% electron-capture decay from ^{197}Tl formed through a ^{197}Au$(\alpha,4n)^{197}$Tl reaction. In this work the formation of ^{197}Hg^g through the genetic decay from ^{197}Tl has been corrected for to obtain the IR's for ^{197}Hg. Similarly, cross sections for ^{198}Au^g only have been reported earlier [11] and not the IR's. The IR's for the ^{197}Au$(\alpha,\alpha'n)^{196}$Au have been recently published [7], but for incident energies below 40 MeV.

The experimental IR's have been analyzed in terms of both PEQ and compound-nucleus theory of nuclear reactions—the motivation being to understand the role

of PEQ emissions in the spin distribution of the residual nuclei. For this purpose we have used the code ALICE/LIVERMORE/85 [14]. The code calculates the PEQ emission spectra from the hybrid model [15–17] and the EQ cross sections from the Weisskopf-Ewing evaporation model [18]. The hybrid model does not calculate the IR's directly and has not been used so far for the study of IR's. Even when the model has been used to analyze the excitation functions of nuclei with a low-lying isomeric state, the IR's themselves were studied in terms of the exciton model with PEQ emissions restricted to a single ejectile [9,10]. The code ALICE/LIVERMORE/85 has the advantage of treating multiple PEQ nucleon emissions. These make significant contributions at higher projectile energies, particularly when proton emissions are involved, as in ^{197}Au$(\alpha,p3n)^{197}$Hg and ^{197}Au$(\alpha,2pn)^{198}$Au reactions.

We use the calculated ejectile energy spectrum to obtain the angular momentum distributions of the intermediate nuclei formed after each successive emission and from them the spin distribution of the final residual nucleus. Various combinations of PEQ and EQ emissions as well as the different sequences in which the ejectiles may be emitted are taken into account to evaluate the average angular momentum distribution of the final nucleus. The IR is obtained from this spin distribution. The experimental procedure is discussed in Sec. II, and the results are presented in Sec. III. The theoretical calculations are discussed in Sec. IV and are compared with the experimental results in Sec. V.

II. EXPERIMENTAL PROCEDURE

The isomers studied in this work were obtained by bombarding ^{197}Au targets by 50-MeV α particles from the Variable Energy Cyclotron Centre, Calcutta, India. The standard stacked foil technique was used to obtain the excitation function of the isomers in the energy range 34–50 MeV. To obtain measurable yields of the long-lived isomers reported in this work, the thickness of the self-supporting ^{197}Au targets was kept relatively high (46.6 mg/cm^2) without significantly affecting the beam energy profile over the target. For the relatively short-lived isomers, 1.0 mg/cm^2 Au deposited on Al foils of thickness 6.9 mg/cm^2 were used as targets. The irradiation times were optimized to the half-lives of the short- and long-lived isomers to ensure their adequate production. The stack, containing not more than three targets, was assembled by arranging 6.85-mg/cm^2 Al foils and ^{197}Au targets in a predetermined sequence. The target and Al spacer foils were of 99.99% purity. The Al spacer foils served as beam energy degraders and internal flux monitors. The irradiation for each set of isomers was performed in duplicate. The energy loss of the α particles in the stack was calculated from the range, energy, and stopping-power tables of Williamson, Boujot, and Picard [19], the beam energy at each foil being taken as the average of entrance and exit energies. A thickly stacked foil may be used to effect a larger energy drop between the first and last target foils and thereby cover a larger energy range of excitation function measurement. How-

ever, as this results in significantly large straggling in the beam energy and, therefore, uncertainties in the projectile energy values at each target, the stacks employed in the present experiment were kept thin.

The projectile flux was obtained (a) by integration of the current from the Faraday cup that held the target using a precalibrated digital current integrator and (b) through the monitor reactions ^{27}Al$(\alpha,3p)^{28}$Mg, ^{27}Al$(\alpha,4p5n)^{22}$Na, and ^{27}Al$(\alpha,4p3n)^{24}$Na using known excitation functions [20]. Typical flux values obtained from the former and average of the latter are, respectively, 1.3×10^{12} and 1.2×10^{12} α particles per sec.

The samples were counted at a fixed geometry on an 8% HPGe detector with a resolution of 2 keV at 1332 keV. The detector was coupled by standard ORTEC electronics to a series-88 CANBERRA multiparameter system. The energy and efficiency calibrations of the detector were carried out using standard sources of ^{125}Sb, ^{133}Ba, and ^{152}Eu of known absolute activities. The sample-to-detector distance of 15 cm ensured that the loss of pulses due to coincidence summing was < 0.3%. The data were analyzed by the SAMPO gamma peak deconvolution program [21]. Inherent amplifier dead-time losses that cannot be compensated by the conventional live-time acquisiton mode of the analyzer arise when the total count rate is high such as those encountered at low cooling times. This was corrected by using an interactive computer-program-based method [22]. Utilizing the relevant nuclear decay scheme data [23] (Table I), the decays of the characteristic gamma peaks were followed for more than five half-lives after the irradiation and the resulting decay plots constructed by linear least-squares regression.

In the case of ^{197}Hg^g, the cross section obtained experimentally (σ_{expt}) is the sum of the contributions from the reaction process (σ_g), the 100% electron-capture decay from ^{197}Tl (σ_{Tl}) and the 91.4% isomeric transition decay from ^{197}Hg^m (σ_m). Since the decay of ^{197}Hg^g was followed after 6 days, i.e., after practically all the ^{197}Tl and ^{197}Hg^m had decayed to ^{197}Hg^g,

$$\sigma_g = \sigma_{\text{expt}} - (\sigma_{\text{Tl}} + 0.914\sigma_m) \ .$$

The cross sections σ_{Tl} were obtained independently.

Cross sections were evaluated along with their statistical errors for each of the duplicate irradiations as well as different signature gammas of the same residual nucleus. The reported cross section is the mean of these values. The error assigned to this mean is the root mean square of the statistical errors associated with the individual cross sections. In addition, there are uncertainties in the beam flux measurements ($\sim3\%$), incident beam energy ($\sim1\%$), and detector efficiencies ($\sim3\%$).

The experimental results can be further affected by two factors. Beam energy degradation may affect the excitation functions in an unpredictable way because of the effects associated with the spread in beam energy. Also, since (α,xn) reactions constitute the dominant channels, secondary neutrons, if produced in large numbers, are likely to interfere with the yields of ^{198}Au and ^{196}Au through the auxiliary ^{197}Au$(n,\gamma)^{198}$Au and

TABLE I. Gamma spectrometric data of nuclides used in the isomer ratio determination [23].

Nuclide	Half-life	Gamma energy with absolute abundances in parenthesis (keV)
^{198}Au^g	2.697 d	412.0 (95.5%)
^{198}Au^m	2.300 d	215.0 (77.0%), 204.0 (41.58%)
^{197}Hg^g	64.130 h	191.3 (0.511%), 268.9 (0.0399%)
^{197}Hg^m	23.800 h	134.0 (34.3%)
^{196}Au^g	6.183 d	333.0 (23.03%), 356.0 (87.6%)
^{196}Au^m	9.700 h	147.7 (43.0%), 188.2 (37.84%), 316.15 (2.924%)
^{197}Tl	2.840 h	152.15 (7.56%), 308.5 (4.356%), 432.9 (2.148%)
^{198}Tl^m	1.870 h	259.6 (2.732%), 260.9 (1.252%), 282.8 (27.05%)
^{198}Tl^g	5.300 h	596.8 (0.9536%), 675.8 (10.4%), 1200.6 (9.214%), 1312.2 (4.524%), 1420.6 (7.6232%)

^{197}Au$(n,2n)^{196}$Au reactions. Both effects are expected to be particularly severe in thickly stacked foils. Although the stack used in this experiment was thin to minimize the beam energy spread, a separate experiment was performed to estimate the contribution of the (n,γ) reaction to the activity of ^{198}Au. The contribution of the $(n,2n)$ reaction to the activity of ^{196}Au can be taken to be negligible since the Q value of the $(n,2n)$ reaction in ^{197}Au is -8.072 MeV and the major portion of the neutron yield in (α,xn) reactions is below 8 MeV for the present energy range of incident alphas [24].

Gold foils of thickness 48.2 mg/cm^2 were wrapped in Al foils of thickness 6.85 mg/cm^2 and fixed to the exterior wall of the irradiation chamber. The position of the foil was off axis to the beam and at an angle backward to the beam-target configurations. The thickness of the chamber wall at this point was 2 mm of stainless steel, and so all 50-MeV alpha particles were stopped. The beam was focused onto a 0.025-mm-thick ^{232}Th target inside the chamber for 6 h at an alpha-projectile current of 2 μA. A more fissile nucleus than ^{197}Au was deliberately chosen as the target so as to ascertain the upper limit of the ^{197}Au$(n,\gamma)^{198}$Au reaction cross section from secondary neutrons. The 411.8-keV gamma of ^{198}Au was followed for a period of 4 days on the same precalibrated detector and counting assembly. As the count rate for the 411.8-keV peak was low, the average counting time was of the order of 10^4 sec. Assuming the neutron-yield spectrum to vary only slightly with the beam energy at this energy range [24], the percentage activities for ^{198}Au produced from background neutrons compared to the alpha activation at energies 35.2, 42.5, 43.9, and 48.6 MeV after correcting for different decay factors and target thicknesses are 0.026%, 0.084%, 0.064%, and 0.03%, respectively. The interference from the secondary neutrons, therefore, can be considered negligible.

III. EXPERIMENTAL RESULTS

The experimental values of IR's for ^{198}Tl, ^{197}Hg, ^{198}Au, and ^{196}Au are shown in Figs. 1–4. The spins and parities

of the isomers are shown in Table II. The error bars are the statistical errors.

A. ^{198}Tl

The IR's of ^{198}Tl have previously been measured with α projectiles on a ^{197}Au target in the energy range of 27–60 MeV [7,11,13]. Figure 1(a) shows that the results obtained in the present work agree, within the limits of experimental error, with the earlier measurements of Lanzafame and Blann [11] and Capurro et al. [13], although the general trend of the former is lower and that of the latter is larger than the present measurements. However, the results of Nagame et al. [7] that cover the energy range of 27–40 MeV are in excess of that of Lanzafame and Blann by approximately an order of magnitude and those of Capurro et al. by factors of 6–7. Scrutiny of the values of Nagame et al. of the cross sections of reaching the isomeric and ground states shows that the cross sections σ_m of ^{198}Tl^m [Fig. 1(d)] are in reasonably good agreement (in the region of overlapping incident energies) with those of Refs. [11] and [13] and the present work. Their cross sections σ_g of ^{198}Tl^g are, however, considerably lower [Fig. 1(c)], and this results in high values of IR's. Figure 1(c) also shows that σ_g of Ref. [11] are larger than those of Ref. [13] and the present work by factors of about 2–4. These large values of σ_g of Ref. [11] are also reflected in the higher values of $\sigma_g + \sigma_m$, as shown in Fig. 1(b).

The disagreement of the σ_g values of Ref. [11] with the

TABLE II. Spin and parities of nuclei.

Reaction	Target	Spin and parities Residual ground state	Residual isomeric state
^{197}Au$(\alpha,3n)^{198}$Tl	$\frac{3}{2}^+$	2^-	7^+
^{197}Au$(\alpha,p3n)^{197}$Hg	$\frac{3}{2}^+$	$\frac{1}{2}^-$	$\frac{13}{2}^+$
^{197}Au$(\alpha,2pn)^{198}$Au	$\frac{3}{2}^+$	2^-	12^-
^{197}Au$(\alpha,\alpha'n)^{196}$Au	$\frac{3}{2}^+$	2^-	12^-
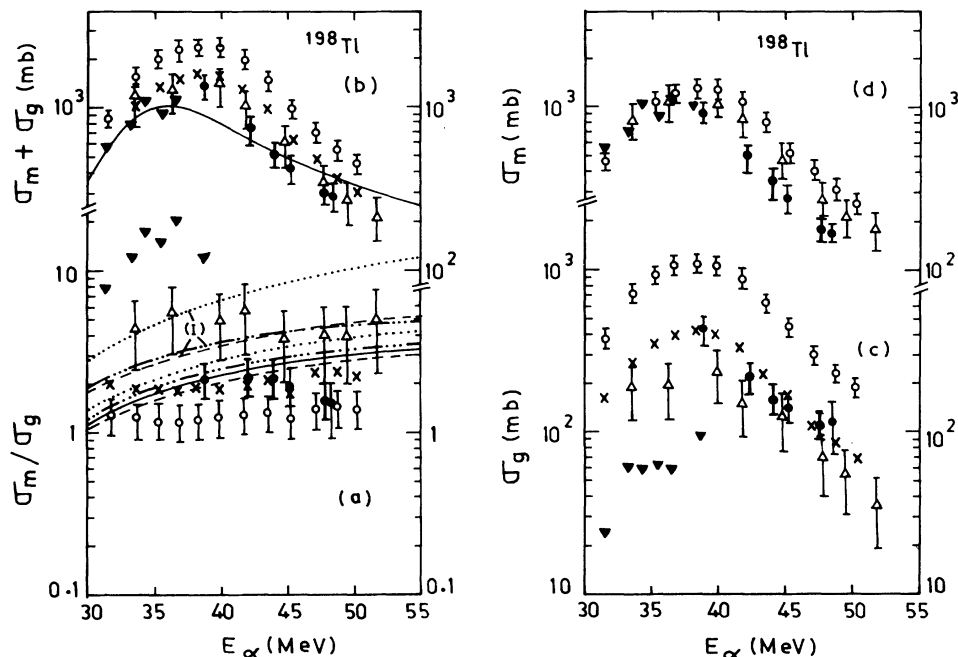
FIG. 1. Excitation functions of (a) σ_m/σ_g, (b) $\sigma_m+\sigma_g$, (c) σ_g, and (d) σ_m for ^{197}Au$(\alpha,3n)$ ^{198}Tl^{m,g} reaction. The measured values are those of Ref. [7] ($\blacktriangledown$), Ref. [11] ($\circ$), corrected values of Ref. [11] ($\times$), Ref. [13] ($\triangle$), and the present work ($\bullet$). The calculated values of σ_m/σ_g are shown in (a) for assumption (A) (dotted curve), assumption (B) (dashed curve), assumption (C) (dot-dashed curve), and assumption (D) (solid curve); calculations with spin cutoff parameter $\sigma^2=\sigma_I$ are marked I and those with $\sigma^2=\sigma_{II}$ are unmarked. The solid line in (b) shows the calculated $\sigma_m+\sigma_g$.

later measurements of Ref. [13] and the present work could arise from the use of old decay scheme data, detector systems of relatively poor resolution, and the use of large stack foils to degrade the incident energy over a wide range. To check the importance of decay schemes, the cross sections of Ref. [11] were reanalyzed using the decay scheme data of the present work [23]. The gamma spectrometric data of Refs. [7] and [13] being concurrent with those of Ref. [23], no such reanalysis is necessary for the σ_m and σ_g values of these authors. The reanalysis results in a marginal reduction of σ_m of Ref. [11] by a factor of about 1.1. More significant is the change in σ_g. These decrease by a factor of about 2.6, which brings the corrected cross sections much closer to those of Ref. [13] and the present work, as shown in Fig. 1(c). The corrected values of $\sigma_m+\sigma_g$ of Ref. [11] are closer to the present measurements and Ref. [13]. The IR values of Ref. [11] are also enhanced by a factor of about 2.5. While the earlier IR's were ~ 1.2, the corrected IR's are now ~ 3, i.e., closer to the present values [Fig. 1(a)].

The very low values of ^{198}Tl^m cross sections of Nagame et al. [7] [Fig. 1(c)] and the corresponding large IR's [Fig. 1(a)] are more difficult to explain. Their gamma spectrometric data are the same as those of the present work and Ref. [13]. To check the validity of our measurements, we used data at 38.8 MeV to obtain in an approximate way the isomeric transition (IT) branching fraction of ^{198}Tl^m. The decay of the 411.8-keV gamma that is contributed to significantly by both ^{198}Tl^m and ^{198}Tl^g was fol-

lowed to obtain the total (sum of the IT and reaction) cross section of ^{198}Tl^g, while the cross section of the shorter-lived ^{198}Tl^m was obtained by peeling off its contribution analytically from the decay curve. With the pure reaction cross section of ^{198}Tl^g roughly obtained from a low-cooling-time analysis of the 675.8-keV gamma, the IT branching fraction was obtained as ~ 0.37, whereas that quoted by Ref. [23] is 0.47. The substitution of Nagame et al., σ_m (~ 1000 mb) and σ_g (~ 94 mb) at 38.7 MeV, resulted in a value of ~ 0.68. In addition, the present σ_g are in better agreement with those of Ref. [13] and the corrected values of Ref. [11] than those of Nagame et al.

The remaining small systematic discrepancies between the present measurements and those of Refs. [11] and [13], particularly for ^{198}Tl^m, may arise from the complexity of the gamma spectrum arising from the decay of ^{198}Tl. The decay of ^{198}Tl results in a complex gamma spectrum because a large number of excited levels of the daughter ^{198}Hg is populated by both the metastable and ground states of ^{198}Tl. In our measurements we were careful to choose [23] (a) the gamma lines of ^{198}Tl^m arising from isomeric transitions alone so that there could be no interference from ^{198}Tl^g, (b) the gamma lines of ^{198}Tl^g following its β^+/EC (electron capture) decay that has no interference from ^{198}Tl^m, and (c) multiple-signature gamma lines, some with energies greater than 1000 keV, so that complications from the Compton background are minimized.

B. ^{197}Hg

The IR's for ^{197}Hg shown in Fig. 2(a) have been measured for the first time. The cross sections of ^{197}Hg^m have been reported earlier in the incident α-energy range of 39–51 MeV [11,12], but no excitation function for ^{197}Au$(\alpha,p3n)^{197}$Hg^g has been reported in literature. Figure 2(b) shows that the trend of the excitation function of ^{197}Hg^m of the present measurements is in fair agreement with that of Refs. [11] and [12], although the present cross sections are larger by factors of 2–3. Figure 2(a) shows that the IR rises rapidly from low values around 35 MeV (the reaction Q value is -29.7 MeV) to near saturation near 40 MeV. The excitation function of $\sigma_m + \sigma_g$ of the present work is shown in Fig. 2(c).

The gamma abundance corrected values of Refs. [11] and [12] show an increase of σ_m of these authors by about 12%, which is not sufficient to account for the discrepancies. Also, these authors use a decay half-life of 24 h compared with the 23.8-h half-life used in the present work. The difference is marginal, but gets accentuated when the decay plot obtained with counts at long cooling times is extrapolated to obtain the zero-time activity. When the decay of the 134-keV gamma of the present work is analyzed with a 24-h half-life, the σ_m values are found to approach those of Refs. [11] and [12], although not strongly enough to remove the disagreements with present measurements. Another factor that may have affected the cross sections of the earlier measurements is the use of thickly stacked foils to obtain large energy degradations (as high as 87 MeV in Ref. [12]), which inevitably result in sizable beam profile broadening. This affects the excitation functions particularly in the energy ranges where the cross sections vary rapidly, as in the near-threshold energies of ^{197}Hg^m investigated presently.

C. ^{198}Au

The presently reported IR's for ^{198}Au in Fig. 3(a) are new. Again, for this nucleus the ^{198}Au^g excitation function has been previously reported by Lanzafame and Blann [11], but no cross section for ^{198}Au^m has been hitherto reported. Figure 3(b) shows the agreement of the present measurements of the cross sections of ^{198}Au^g with those of Ref. [11]. Figure 3(a) shows that the values of IR's are low and practically constant in the energy range investigated. The measured values of $\sigma_m + \sigma_g$ are shown in Fig. 3(c).

Figure 3(b) shows the agreement of the present measurements of the cross sections of ^{198}Au^g with those of Ref. [11]. The σ_g values of Ref. [11] are systematically a little higher than the present values. The disagreement is larger in the lower-incident-energy range. The decay scheme data is the same in both measurements. However, the use of thickly stacked foils in the earlier measurements would lead to uncertainties in the projectile energy on the target foils, particularly at lower energies, as a consequence of larger beam energy straggling. That this may be a significant reason for the discrepancies is suggested by the increasing disagreement with decreasing energy.
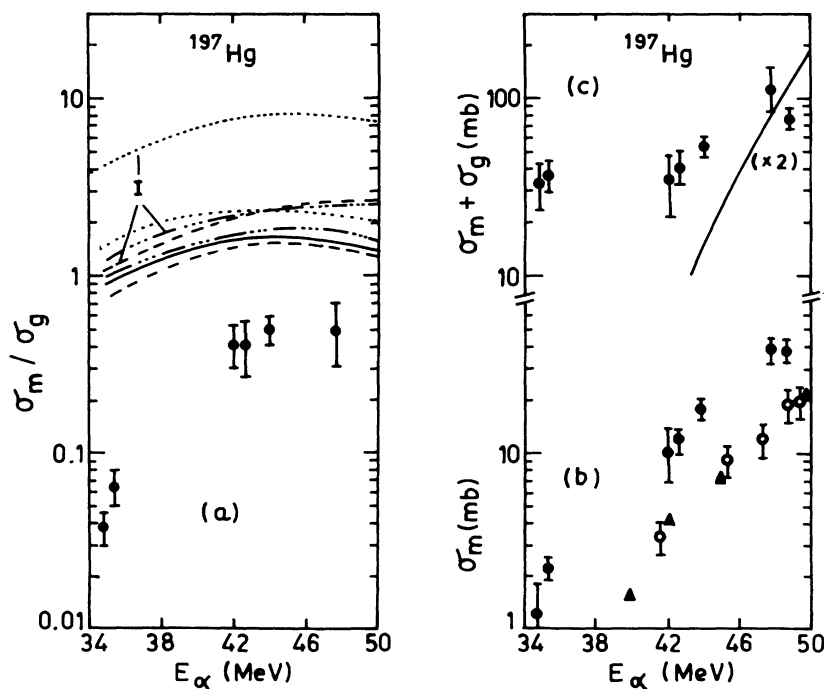

FIG. 2. Same as Fig. 1 for the ^{197}Au$(\alpha,p3n)$ ^{197}Hg^{m,g} reaction. The measured values are those of Ref. [11] ($\circ$), Ref. [12] ($\blacktriangle$), and present work ($\bullet$).
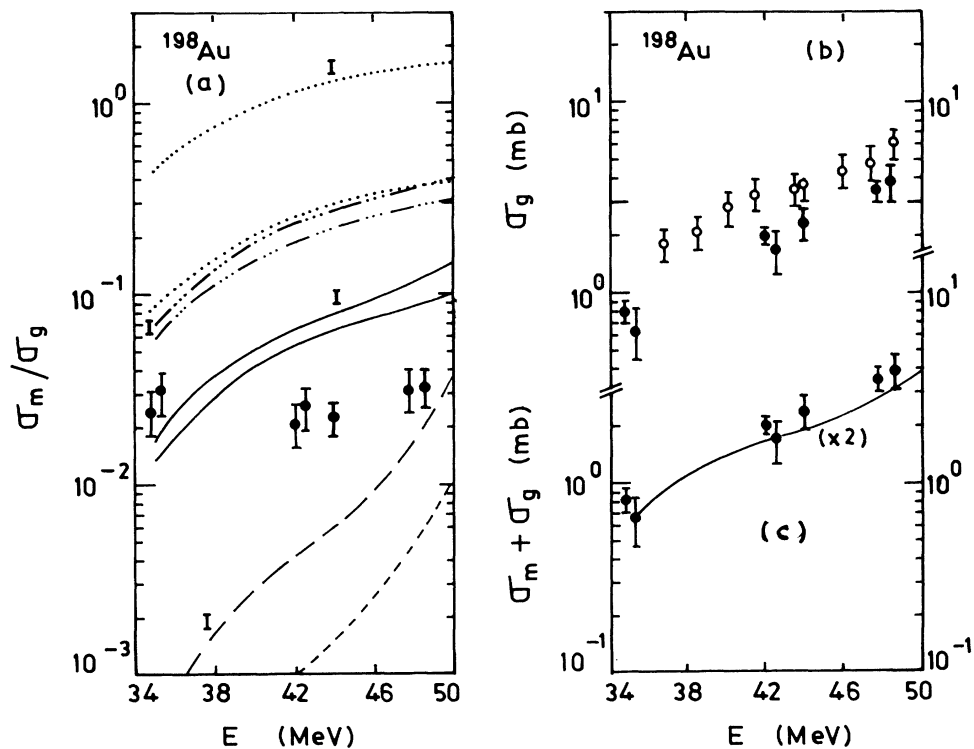
FIG. 3. Same as Fig. 1 for the ^{197}Au($\alpha,2pn$) ^{198}Au^{m,g} reaction.

D. ^{196}Au

For ^{196}Au we report the excitation function of IR's from 34 to 50 MeV in Fig. 4. Nagame et al. [7] have also reported the IR's for ^{196}Au, but for lower incident α ener-

gies of 23–36 MeV. The excitation functions of ^{196}Au^g were studied earlier by Lanzafame and Blann [11] in the energy range 25–51 MeV. The energy range of Nagame et al. and ours overlap only at 34–36 MeV. Figure 4(a) shows that their IR's at these energies are higher than
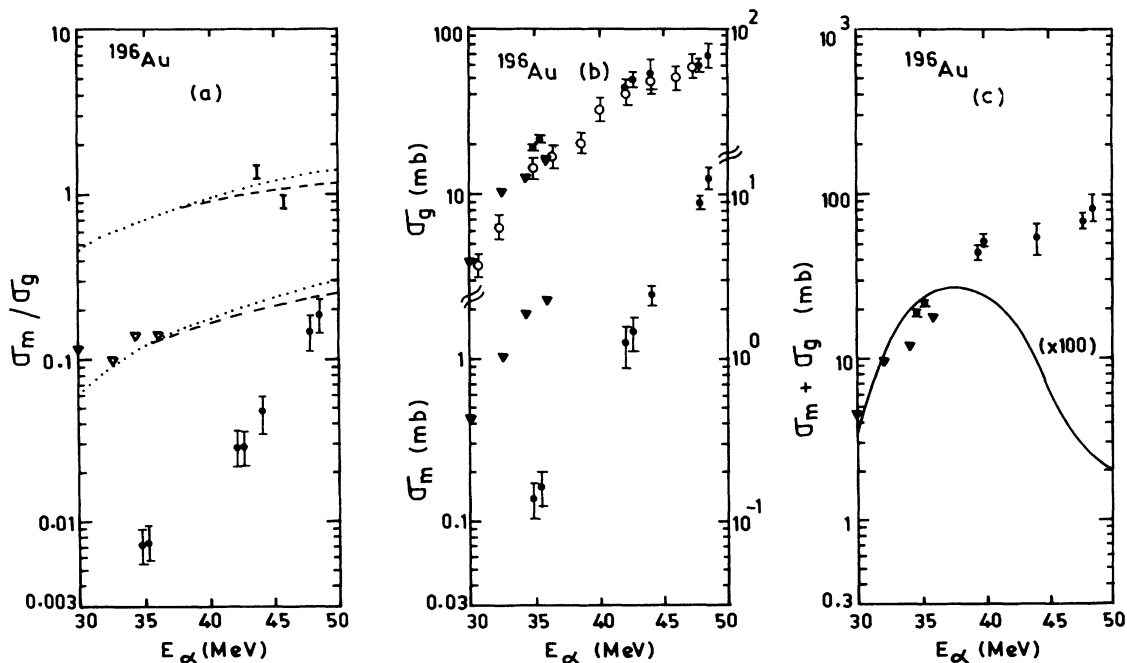

FIG. 4. Same as Fig. 1 for the ^{197}Au($\alpha,\alpha'n$) ^{196}Au^{m,g} reaction.

ours by an order of magnitude. Judging by the trend of our values, which displays a decrease as the energy is reduced, the discrepancy between the IR's of Nagame *et al.* and ours at energies around 30 MeV is expected to be even larger. Figure 4(b) shows the comparison of the excitation function of $^{196}Au^g$ of Refs. [7], [11], and the present work, as well as the excitation function of $^{196}Au^m$ as measured by us and Ref. [7]. While all three excitation functions of $^{196}Au^g$ are in good agreement, the cross sections of $^{196}Au^m$ of Nagame *et al.* around 35 MeV exceed ours by an order of magnitude, resulting in the discrepancies in the IR's of the two experiments. The values of σ_m are about an order of magnitude less than the corresponding values of σ_g. As a result, the difference between the $\sigma_m + \sigma_g$ values of Nagame *et al.* and the present work as shown in Fig. 4(c) are not as large as in the case of IR's.

The values of Nagame *et al.* need no gamma abundance correction as their values are concurrent with those used in the present work. Since they have performed a chemical separation to analyze the Au residuals, the question of interference from neighboring gamma rays does not arise. In the present experiment no chemical separation was done for Au, but it can be seen [23] that with the present detector resolution interference from residuals other than Au is ruled out for the three signature gammas used (Table I). However, for the 316.2-keV gamma, interference from the 316.5-keV (78.3% abundance) gamma from $^{197}Au(\alpha,\alpha 5n)^{192}Au$ cannot possibly be ruled out. But corrections, if necessary, for this interference would reduce the σ_m values and thereby increase the disagreement with those of Ref. [7]. However, this effect is negligible because the cross sections from all three signature gammas are in good agreement.

Insufficient off-line analysis details (eg., detector resolution, duration of irradiation, etc.) in Ref. [7] preclude further comments. An independent analysis along the lines of that done for $^{198}Tl^g$ (Sec. III A) is also ruled out since the $^{196}Au^m$ cross sections are too small to cause discernible variations in the cross sections of $^{196}Au^g$ produced from both IT's and reaction over the $^{196}Au^g$ cross section formed through the reaction along.

IV. MODEL CALCULATIONS

For a theoretical analysis of the observed IR's in terms of PEQ emissions, we have used the hybrid model [15] and the related geometry-dependent hybrid (GDH) model [16]. The latter takes into account the effects of the reduced nuclear density and potential at the nuclear surface for the early stages of PEQ emissions. In a later modification of the model [17], PEQ emission of more than one nucleon has been introduced. Multiple PEQ emissions can be of two types: simultaneous and sequential. In the former two or more nucleons can be emitted from the same exciton state (characterized by the number of excited particles and holes), while in the latter one or more intranuclear transitions occur between emissions so that the emissions take place from different exciton states of different nuclei. We have used the code

ALICE/LIVERMORE/85 of Blann [14] to obtain the PEQ and EQ spectra of ejectiles. The code calculates the PEQ nucleon emission spectra using the hybrid model with the option of GDH model calculation from the initial exciton state and simultaneous PEQ emission of two nucleons. It does not, however, include PEQ emission of clusters. Cluster emissions are included in the EQ component of the reaction where the code uses the standard Weisskopf-Ewing model [18] to calculate proton, neutron, deutron, and alpha emission spectra. From the calculated PEQ and EQ spectra, we calculate the average spin distribution of the final nucleus and the IR's as described below.

A. Initial spin distribution

The angular momentum distribution of the final nucleus is determined by the spin distributions of the target and projectile composite nucleus and the intermediate nuclei formed after each emission. The probability $P(E_c, J_c)$ of the composite nucleus having spin J_c at excitation E_c is [2]

$$P(E_c, J_c) = \frac{\sigma_c(E_c, J_c)}{\sum_{J_c} \sigma_c(E_c, J_c)}$$

$$= \frac{\pi \chi^2 (2J_c + 1)}{(2I + 1)(2s + 1)\sigma_{abs}}$$

$$\times \sum_{j = |I - s|}^{I + s} \sum_{l = |J_c - j|}^{J_c + j} T_l(E) , \qquad (1)$$

where $\sigma_c(E_c, J_c)$ is the formation cross section of the composite nucleus with spin J_c and $\sum \sigma_c(E_c, J_c)$ is the absorption cross section σ_{abs} of the projectile by the target. χ is the reduced de Broglie wavelength of the projectile with energy E. s and l are, respectively, its intrinsic spin and orbital angular momentum. $T_l(E)$ is the transmission coefficient of the projectile, and I is the spin of the target. $P(E_c, J_c)$ is normalized by $\sum_{J_c} P(E_c, J_c) = 1$.

The first intermediate nucleus is formed with spin J_1 at an excitation E_1 when the first ejectile having intrinsic spin s_1 is emitted with energy ε_1 and orbital angular momentum l_1. The excitation $E_1 = E_c - B_1 - \varepsilon_1$, where B_1 is the ejectile separation energy. The values of J_c that can populate a given J_1 are $|J_1 - l_1'| \leq J_c \leq J_1 + l_1'$, where $|l_1 - s_1| \leq l_1' \leq l_1 + s_1$. The probability $P(E_1, J_1)$ of the intermediate nucleus being formed in the spin state J_1 is determined by the angular momentum carried away by the ejectile, i.e., by its energy ε_1 and its angular distribution.

B. Spin distribution for equilibrium emission

For EQ emission with isotropic angular distribution, the probability of reaching J_1 depends on the phase space available to the given J_1 relative to the total phase space available to all spin states that can be reached through the same combination of J_c, l_1', and ε_1. If $\rho(E_1, J_1)$ is the density of states with spin J_1 at excitation E_1, then this factor is the ratio

$$\frac{\rho(E_1,J_1)}{\sum_{J_1}\rho(E_1,J_1)} = \frac{f(J_1)}{\sum_{J_1=|J_c-l_1'|}^{J_c+l_1'} f(J_1)} , \qquad (2)$$

where

$$\rho(E_1,J_1) = \rho(E_1)\frac{(2J_1+1)\exp[-J_1(J_1+1)/2\sigma^2]}{2\sqrt{2\pi}\sigma^3}$$

$$= \rho(E_1)f(J_1) , \qquad (3)$$

$\rho(E_1)$ being the spin-integrated level density and σ^2 the spin cutoff parameter. $P(E_1,J_1)$ also depends on the probability $P(\varepsilon_1)$ of the ejectile having energy ε_1. This is obtained from the energy differential cross section $\sigma(\varepsilon_1)$:

$$P(\varepsilon_1) = \frac{\sigma(\varepsilon_1)}{\int d\varepsilon_1 \sigma(\varepsilon_1)} . \qquad (4)$$

Other factors that determine $P(E_1,J_1)$ are the probability of any l_1' occurring for a given l_1 and the probability with which l_1 occurs for a given ε_1. The former is $1/(2s_1+1)$, and the latter is given by the ratio $T_{l_1}(\varepsilon_1)/\sum_{l_1=0}^{\infty}T_{l_1}(\varepsilon_1)$, $T_{l_1}(\varepsilon_1)$ being the ejectile transmission coefficient.

Combining all these factors,

$$P(E_1,J_1)=P(\varepsilon_1)\sum_{l_1=0}^{\infty}\left[T_{l_1}(\varepsilon_1)\bigg/\sum_{l_1=0}^{\infty}T_{l_1}(\varepsilon_1)\right]\sum_{l_1'=|l_1-s_1|}^{l_1+s_1}\sum_{J_c=|J_1-l_1'|}^{J_1+l_1'} P(E_c,J_c)f(J_1)\bigg/\left[(2s_1+1)\sum_{J_1=|J_c-l_1'|}^{J_c+l_1'}f(J_1)\right] . \qquad (5)$$

The energy-averaged spin distribution is

$$P(J_1)=\int dE_1 P(E_1,J_1) , \qquad (6)$$

with the normalization $\sum P(J_1)=1$.

For successive EQ emissions, the spin distribution $P(E_N,J_N)$ of the Nth nucleus is calculated from (5) by replacing ε_1 and s_1 by the energy ε_N and intrinsic spin s_N of the relevant ejectile and $P(E_c,J_c)$ by $\int d\varepsilon_N P(E_{N-1},J_{N-1})$, where $P(E_{N-1},J_{N-1})$ is the spin distribution of the previous nucleus. The integration over ε_N together with the condition that $\varepsilon_N=E_N+B_N-E_{N-1}$ ensures that all values of E_{N-1} and ε_N that can populate a given E_N are taken into account.

C. Spin distribution for pre-equilibrium emission

The PEQ emissions are characterized by the presence of high-energy ejectiles in the emission spectrum and forward-peaked angular distribution. The effect of angular momentum on the emission spectrum is not included either in the hybrid model or other semiclassical models of PEQ emissions. The forward-peaked angular distribution is described either phenomenologically [25] or through linear momentum conservation in the intranuclear cascade of two-body interactions [26,27]. We therefore use a number of extreme assumptions to evaluate the spin distribution following PEQ emission.

(A) The PEQ ejectiles have the same angular distribution as in EQ emission. This assumption has been used by several authors [4,9,10]. In this case $P(E_1,J_1)$ is evaluated from (5). The effect of PEQ ejectiles carrying higher energy is included in the evaluation of $P(\varepsilon_1)$ from (4) in terms of PEQ energy spectra.

(B) If the intrinsic spin of the projectile, target, and ejectile is neglected, then $\mathbf{J}_c=\mathbf{l}$ and $\mathbf{J}_1=\mathbf{J}_c-\mathbf{l}_1$. If, in addition, we include the effect of the predominantly forward-angle emissions of PEQ ejectiles through the extreme assumption that all PEQ emissions take place along the incident direction, then $\mathbf{J}_c$ (or $\mathbf{l}$) and $\mathbf{l}_1$ are parallel and

$$J_1=J_c-l_1 . \qquad (7)$$

In this case maximum angular momentum is removed by PEQ emission. A further assumption is made that the impact parameters of the projectile and ejectile are same; i.e., all PEQ emissions take place through a single-step interaction between the projectile and target. This restricts the values of the ejectile angular momentum to

$$l_1=J_c\left[\frac{m_1\varepsilon_1}{mE}\right]^{1/2} , \qquad (8)$$

where m_1 and m are the ejectile and projectile masses, respectively. $P(E_1,J_1)$ is then given by

$$P_B(E_1,J_1)=P(\varepsilon_1)\sum_{J_c=|J_1-l_1|}^{J_1+l_1}P(E_c,J_c)\delta_{J_1,J_c-l_1} , \qquad (9)$$

where the Kronecker δ function ensures that the restriction imposed by (7) is taken into account. $\sum_{J_1}\int dE_1 P_B(E_1,J_1)=1$ is the normalization.

These extreme assumptions have been used by Bissem et al. [9] and Marten et al. [10] to investigate the IR's for proton- deuteron- and ^{3}He-induced reactions. As has been pointed out by these authors, the assumptions are more justified the larger the projectile mass.

In (9) the transmission coefficients $T_{l_1}(\varepsilon_1)$ do not occur explicitly for the following reasons. First, (7) allows only a single value of l_1 for given J_1 and J_c. Second, as the impact parameter for the ejectile is assumed to be the same as that of the projectile, the probability of the ejectile having orbital angular momentum l_1 is given by $P(\varepsilon_1)$ [see (8)]. In other words, the probability of l_1 occurring for a given ε_1 is unity when $T_{l_1}(\varepsilon_1)>0$; when $T_{l_1}(\varepsilon_1)=0$, we make $\sigma(\varepsilon_1)=0$ in (4).

(C) The spins J_c and l_1 are parallel as in (B), but the ejectile impact parameters are not restricted to the projectile impact parameters only; i.e., l_1 is no longer evaluated from (8). Instead, all values of l_1 with probability $T_{l_1}(\varepsilon_1)/\sum_{l_1'=0}^{\infty}T_{l_1'}(\varepsilon_1)$ can contribute to the formation of

J_1 and

$$P_c(E_1,J_1)$$

$$= P(\varepsilon_1) \sum_{l_1=0}^{\infty} \left[T_{l_1}(\varepsilon_1) \bigg/ \sum_{l_1'=0}^{\infty} T_{l_1'}(\varepsilon_1) \right]$$

$$\times \sum_{J_c=|J_1-l_1|}^{J_1+l_1} P(E_c,J_c) \delta_{J_1,J_c-l_1} \ . \qquad (10)$$

The normalization of $P_c(E_1,J_1)$ is as in (9). The angular momentum carried away is less when (10) is used than (9).

(D) Assumption (B) in effect considers PEQ emissions to take place from the initial exciton state n_0, characterized by the number of excited particles and holes created immediately after the absorption of the projectile. On the other hand, (C) considers emissions from all exciton states. Although emissions from n_0 may constitute the major part of the PEQ spectrum, emission from other exciton states cannot be neglected. A weighted sum of (9) and (10) is used to obtain the spin distribution. The probability $W(n_0)$ of PEQ emissions from n_0 alone is given by the ratio of the emission cross section from n_0 to the total PEQ cross section of the relevant ejectile. The PEQ emission cross section from n_0 is obtained from the code ALICE/LIVERMORE/85 by restricting the GDH calculations to emissions from n_0 followed by hybrid model calculations for the higher exciton states:

$$P_D(E_1,J_1) = W(n_0)P_B(E_1,J_1)$$

$$+ [1 - W(n_0)]P_C(E_1,J_1) \ . \qquad (11)$$

The spin distribution of the nucleus formed after simultaneous PEQ emission of two nucleons is calculated as in the case of sequential emission by assuming that a virtual intermediate nucleus is formed through emission of one of the two nucleons. When two like nucleons are emitted simultaneously, the virtual nucleus is the same for either of the emitted particles. For the simultaneous emission of a proton and a neutron, the two different virtual nuclei are assumed to be formed with equal probability. The model calculates the total PEQ proton and total PEQ neutron spectra, i.e., the energy spectrum of a proton (neutron) emitted singly as well as simultaneously with another nucleon [17]. For the formation of the virtual nucleus with excitation E_1, all values of ejectile energy up to $E_c - E_1 - B_1$ are taken into account. For the nucleus formed with excitation E_2 after simultaneous PEQ emission, the maximum ejectile energy is $E_1 - E_2 - B_2$.

D. Multiple-particle emission

Equations (5), (9), and (10) describe the spin distribution following the first emission. In the case of multiple emissions, the reaction can proceed through a number of channels. For instance, in the case of a neutron and a proton, the proton may be emitted first followed by a neutron or vice versa. Again, both ejectiles may undergo EQ emission or both may be PEQ ejectiles or a PEQ emission of one may be followed by the EQ emission of

the other. The reaction proceeds through the different channels with different probabilities. Successive use of (5) gives the final nucleus spin distribution for the channel in which only EQ emissions occur. Similarly, use of (9) or (10) with (5) gives the spin distribution reached through the channel in which PEQ is followed by EQ emission. The average spin distribution is the weighted sum of the distribution from each channel, and to obtain this average it is necessary to evaluate the relative probabilities of the different channels. We describe the calculations of these relative probabilities for the reaction $^{197}\text{Au}(\alpha,3n)$ ^{198}Tl as an illustration.

In this reaction, ^{198}Tl is formed through the following channels. Channel 1, simultaneous PEQ emission of two neutrons from the composite nucleus ^{201}Tl followed by EQ neutron emission from ^{199}Tl; channel 2, PEQ neutron emission from ^{201}Tl followed by successive neutron emissions from ^{200}Tl and ^{199}Tl; channel 3, successive EQ emissions for all three neutrons. There are also other possible channels through which the reaction can proceed; e.g., all three neutrons undergo PEQ emission either simultaneously or sequentially. Since the code calculates PEQ spectra for up to two simultaneous nucleon emissions, we do not consider these other channels.

Denoting the probability and cross section of the formation of the (Z, A) nucleus though the ith channel by $\mathcal{P}_i(Z, A)$ and $\sigma_i(Z, A)$, respectively, the probability, $\mathcal{P}_i(^{199}\text{Tl})$, of formation of ^{198}Tl, is

$$\mathcal{P}_i(^{198}\text{Tl}) = \frac{\sigma_i(^{198}\text{Tl})}{\sum_{i=1}^{3} \sigma_i(^{198}\text{Tl})} \ , \qquad (12)$$

with $\sum_{i=1}^{3} \mathcal{P}_i(^{198}\text{Tl}) = 1$.

In all three channels, ^{198}Tl is formed through EQ neutron emission from ^{199}Tl and

$$\sigma_i(^{198}\text{Tl}) = \mathcal{P}_i(^{199}\text{Tl})\sigma_{EQ}^n(^{199}\text{Tl}) \ , \qquad (13)$$

where $\sigma_{EQ}^n(^{199}\text{Tl})$ is the EQ neutron emission cross section from ^{199}Tl and $\mathcal{P}_i(^{199}\text{Tl})$ is given as in (12) by

$$\mathcal{P}_i(^{199}\text{Tl}) = \frac{\sigma_i(^{199}\text{Tl})}{\sum_{i=1}^{3} \sigma_i(^{199}\text{Tl})} \ . \qquad (14)$$

In channel 1, ^{199}Tl is formed through the simultaneous PEQ emission of two neutrons from ^{201}Tl. Writing $\sigma_{PEQ}^{nn}(^{201}\text{Tl})$ as the cross section of this process.

$$\sigma_1(^{199}\text{Tl}) = \sigma_{PEQ}^{nn}(^{201}\text{Tl}) \ . \qquad (15)$$

In channels 2 and 3, ^{199}Tl is formed through the EQ neutron emission from ^{200}Tl, which in turn is formed in channel 2 through PEQ neutron emission and in channel 3 from EQ neutron emission from ^{201}Tl. Consequently,

$$\sigma_2(^{199}\text{Tl}) = \frac{\sigma_{PEQ}^n(^{201}\text{Tl})\sigma_{EQ}^n(^{200}\text{Tl})}{\sigma_{PEQ}^n(^{201}\text{Tl}) + \sigma_{EQ}^n(^{201}\text{Tl})} \ , \qquad (16)$$

$$\sigma_3(^{199}\text{Tl}) = \frac{\sigma_{EQ}^n(^{201}\text{Tl})\sigma_{EQ}^n(^{200}\text{Tl})}{\sigma_{PEQ}^n(^{201}\text{Tl}) + \sigma_{EQ}^n(^{201}\text{Tl})} \ , \qquad (17)$$

$$\sigma_2(^{199}\text{Tl}) + \sigma_3(^{199}\text{Tl}) = \sigma_{EQ}^n(^{200}\text{Tl}) \ , \qquad (18)$$

where $\sigma_{EQ}^n(^{201}Tl)$ and $\sigma_{EQ}^n(^{200}Tl)$ are the EQ neutron emission cross sections from ^{201}Tl and ^{200}Tl, respectively, and $\sigma_{PEQ}^n(^{201}Tl)$ is the PEQ neutron emission cross section from ^{201}Tl. From (12)–(18) we have

$$\mathcal{P}_1(^{198}Tl) = \frac{\sigma_{PEQ}^{nn}(^{201}Tl)}{\sigma_{PEQ}^{nn}(^{201}Tl) + \sigma_{EQ}^n(^{200}Tl)} , \tag{19}$$

$$\mathcal{P}_2(^{198}Tl) = \frac{\sigma_{PEQ}^{n}(^{201}Tl)}{\sigma_{PEQ}^{n}(^{201}Tl) + \sigma_{EQ}^n(^{201}Tl)}$$
$$\times \frac{\sigma_{EQ}^{n}(^{200}Tl)}{\sigma_{PEQ}^{nn}(^{201}Tl) + \sigma_{EQ}^n(^{200}Tl)} , \tag{20}$$

$$\mathcal{P}_3(^{198}Tl) = \frac{\sigma_{EQ}^{n}(^{201}Tl)}{\sigma_{PEQ}^{n}(^{201}Tl) + \sigma_{EQ}^n(^{201}Tl)}$$
$$\times \frac{\sigma_{EQ}^{n}(^{200}Tl)}{\sigma_{PEQ}^{nn}(^{201}Tl) + \sigma_{EQ}^n(^{200}Tl)} , \tag{21}$$

as the formation probabilities of ^{198}Tl through each of three channels. $\sigma_{PEQ}^{nn}(^{201}Tl)$, $\sigma_{PEQ}^n(^{201}Tl)$, $\sigma_{EQ}^n(^{201}Tl)$, and $\sigma_{EQ}^n(^{200}Tl)$ are obtained from the code.

Similar considerations apply in evaluating the relative formation probabilities of ^{197}Hg, ^{198}Au, and ^{196}Au. The number of possible channels through which these nuclei may be formed are more than those of ^{198}Tl because there are more ejectiles, and also because some of the ejectiles are distinguishable. Thus ^{197}Hg can be formed through 11 channels by the $(\alpha,p3n)$ reaction, while ^{198}Au can be formed through 8 channels by the $(\alpha,2pn)$ reaction and by further 2 channels (PEQ and EQ) of the $(\alpha,^3He)$ reaction. The last has not been considered as the code does not take into account the emission of ^3He. For the formation of ^{198}Au, 30 channels are available through $(\alpha,2p3n)$ and $(\alpha,\alpha'n)$ reactions. The Q value of the former is -36.33 MeV and of the latter -8.07 MeV. As a result, contributions from $(\alpha,2p3n)$ reactions are very small for incident energies up to 50 MeV. Consequently, we have considered only 3 channels for the formation of ^{196}Au through the $(\alpha,\alpha'n)$ reaction only. A fourth channel in which a PEQ α emission is followed by EQ neutron emission has been ignored since the hybrid model does not treat PEQ cluster emissions. All the channels considered in the calculations are listed in Table III.

The average spin distribution of the (Z, A) nucleus is

TABLE III. List of channels through which ^{198}Tl, ^{197}Hg, ^{198}Au, and ^{196}Au are formed. PEQ and EQ denote pre-equilibrium and equilibrium emissions respectively. p stands for proton, n for neutron, and α for alpha particle. (pn), (pp), and (nn) signify simultaneous emissions of proton and neutron, two protons, and two neutrons, respectively.

Nucleus	Channel number	First emission	Second emission	Third emission	Fourth emission
^{198}Tl	1	PEQ (nn)	EQ n		
	2	PEQ n	EQ n	EQ n	
	3	EQ n	EQ n	EQ n	
^{197}Hg	1	PEQ (pn)	EQ n	EQ n	
	2	PEQ p	EQ n	EQ n	EQ n
	3	EQ p	EQ n	EQ n	EQ n
	4	PEQ n	EQ p	EQ n	EQ n
	5	EQ n	EQ p	EQ n	EQ n
	6	PEQ (nn)	EQ p	EQ n	
	7	PEQ n	EQ n	EQ p	EQ n
	8	EQ n	EQ n	EQ p	EQ n
	9	PEQ (nn)	EQ n	EQ p	
	10	PEQ n	EQ n	EQ n	EQ p
	11	EQ n	EQ n	EQ n	EQ p
^{198}Au	1	PEQ (pp)	EQ n		
	2	PEQ p	EQ p	EQ n	
	3	EQ p	EQ p	EQ n	
	4	PEQ (pn)	EQ p		
	5	PEQ p	EQ n	EQ p	
	6	EQ p	EQ n	EQ p	
	7	PEQ n	EQ p	EQ p	
	8	EQ n	EQ p	EQ p	
^{196}Au	1	PEQ n	EQ α		
	2	EQ n	EQ α		
	3	EQ α	EQ n		

$$\overline{P(E_N,J_N)}= \sum_i \mathcal{P}_i(Z,A)P_i(E_N,J_N) \ , \qquad (22)$$

where $P_i(E_N,J_N)$ is the spin distribution of the (Z,A) nucleus when formed through the ith channel with excitation E_N and spin J_N. $P_i(E_N,J_N)$ is evaluated from the appropriate combination of (9) or (10) with (5). The energy-integrated average spin distribution is given by

$$\overline{P(J_N)}= \sum_i \mathcal{P}_i(Z,A)P_i(J_N) \ , \qquad (23)$$

where $P_i(J_N)$, the energy-integrated spin distribution for the ith channel, is given by (6).

E. Gamma emission

After particle emissions the final nucleus is formed with excitation energy less than the particle emission threshold. It then de-excites through continuum-to-continuum and continuum-to-discrete state gamma transitions. The strength functions of the gammas of different multipolarity determine the relative branching probabilities to the metastable and ground states. The IR depends on both the final nucleus spin distributions and the relative gamma branching probabilities. The former is independent of the latter. The same gamma branching will result in different IR's for different spin distributions. In order to investigate the importance of the reaction mechanism on the spin distribution and thereby on the IR's, we have used a simplified approach to calculate the relative population of the isomeric and ground states by gamma de-excitation. For all the four nuclei studied, the spin of the metastable state is larger, and we assume that those states which have spin less than the spin J_m of the metastable state exclusively populate the ground state, while all other states decay to the isomeric state. With this sharp division assumption, the gamma branching probabilities are independent of the excitation energy and one can use the energy-integrated average spin distribution of (23) to obtain the IR's as

$$\frac{\sigma_m}{\sigma_g} = \sum_{J_N=J_m}^{\infty} \overline{P(J_N)} \bigg/ \left[1 - \sum_{J_N=J_m}^{\infty} \overline{P(J_N)} \right] \ . \qquad (24)$$

This sharp division assumption of relative gamma transitions has been used by Grant and Rathle [6] for analysis of IR's from (α,xn) and (α,pn) reactions on In and Sn isotopes. Other authors [7,8,10] have also used this assumption to study the effect of entrance channel spin distribution on IR's of multiple-neutron-emission reactions with protons, deuterons, triton, ^{3}He, and alpha projectiles.

V. COMPARISONS BETWEEN CALCULATIONS AND EXPERIMENT

A. Input parameters

To obtain the emission spectra from the code ALICE/LIVERMORE/85, all the input parameters were generated internally. The code calculates the reaction Q values from the experimental masses of Mattauch, Thiele,

and Wapstra [28] wherever available and from the Myers-Swiatecki mass formula [29] in all other cases. For calculating the pairing corrections in level densities, we use the option whereby the pairing term for a nucleus with mass number A is zero for odd-even, $11/(A)^{1/2}$ for even-even, and $-11/(A)^{1/2}$ for odd-odd nuclei. The pairing correction is subtracted from the excitation energy. The code does not provide the option for using individual level-density parameters for particular residual nuclides. It calculates the level-density parameter ($\pi^2/6$ times the single-particle level density) in terms of the compound-nucleus mass number A_c as $(A_c-x)/C$, where C is a constant and $x=1$, 2, and 4 for nucleon, deuteron, and alpha ejectiles, respectively. We have used $C=15$ instead of the default parameter $C=9$.

For PEQ nucleon emission calculations, the initial number of excited particles and holes is an important input parameter. We have used the default option provided in the code for alpha projectiles whereby the initial number of excited neutrons and protons are each taken as 2. After each two-body interaction, the number of excited neutrons and protons each increases by 0.5 so that the total number of excited particles increases by 1. The two-body collision rate λ_+, which competes with PEQ emissions, is calculated from the empirical closed-form expression [15,16]

$$\lambda_+ = [1.4\times10^{21}(\varepsilon+B)-6\times10^{18}(\varepsilon+B)^2]k^{-1} \ \text{sec}^{-1} \ ,$$

where B is the ejectile separation energy and k is an adjustable constant which accounts for the decrease in the two-body collision rate due to the Pauli correction of the two-body scattering cross section. We have used $k=3.5$, as then λ_+ corresponds to the two-body interaction rates obtained from the Becchetti-Greenlees optical-model potential [27]. For alpha projectiles the code calculates the entrance-channel transmission coefficients $T_l(E)$ from the Hill-Wheeler expression for the penetrability of a parabolic barrier using the parameters of Huizenga and Igo [30]. The inverse reaction cross sections in the exit channels were generated internally by a classical sharp cutoff model.

B. Results on excitation functions

The hybrid model has been used to analyze the excitation functions for a wide variety of reactions. The model has been fairly successful in describing proton-induced reactions [31]. For alpha-induced reactions the model has had mixed success. It does show good agreement with (α,xn) and some $(\alpha,xnyp)$ reactions [8,32], but severe discrepancies have also been reported in some cases [33]. Similar features are seen in our excitation function calculations also. The cross sections for ^{197}Au$(\alpha,3n)^{198}$Tl reactions show satisfactory agreement with experiment [Fig. 1(b)], while for ^{197}Au$(\alpha,2pn)^{198}$Au the trend of the excitation function is fairly well reproduced though the absolute values of the cross sections are underpredicted by a factor of 2 [Fig. 3(c)]. For ^{197}Au$(\alpha,p3n)^{197}$Hg [Fig. 2(c)] and ^{197}Au$(\alpha,\alpha'n)^{196}$Au [Fig. 4(c)], on the other hand, neither the calculated cross sections nor the trend of the excitation function

have been reproduced. In the case of the latter, the neglect of PEQ alpha cluster emission may be a strong reason for the failure of the hybrid model, particularly for higher energies where calculations show a decrease in the cross sections in contrast to experiment.

The excitation function calculations are influenced by the reaction mechanisms. In the model calculations for ^{197}Hg, ^{198}Au, and ^{196}Au, only nucleon emissions are considered in the PEQ channels. PEQ cluster emissions will affect the formation cross sections of these nuclei, and the neglect of these emissions in the hybrid model may be a likely reason for the discrepancies between the observed and calculated excitation functions. Cluster emissions are not involved in the ^{197}Au$(\alpha,3n)^{198}$Tl reaction, and the agreement of the model calculations with experiment is satisfactory.

There may be other important reasons for the failure of the hybrid model for some alpha-induced reactions. Reaction cross sections are dependent on the inverse cross sections and the density of states available to the reaction product. A proper parametrization of these factors, particularly the level-density parameter which strongly influences the reaction cross section, is essential for the successful prediction of reaction cross sections. For instance, use of the default-option level-density parameter constant $C=9$ results in significant underprediction (sometimes by one or two orders of magnitude) of the cross sections compared with the present calculations with $C=15$. However, the IR is not sensitive to the level-density parameter.

C. Results on isomer ratios

The IR depends on the relative spin distribution of the reaction product and on the relative gamma branching to the isomeric and ground states. The important parameter for evaluating the spin distribution is the spin cutoff parameter σ^2, which is related to the nuclear moment of inertia $\mathcal{I}$, as $\sigma^2 = \mathcal{I} T / \hbar^2$, where T is the nuclear temperature. For our calculations we have used two values of σ^2: one corresponding to half the rigid-body moment of inertia and the other a constant value of $\sigma^2 = 10$. These are subsequently referred in the text as σ_I and σ_{II}, respectively.

The probability $\mathcal{P}_i(Z, A)$ of the residual nucleus (Z, A) being formed through channel i plays an important role in determining the relative spin distribution [Eqs. (22) and (23)]. The values of $\mathcal{P}_i(Z, A)$ are model dependent. In the present calculations of the hybrid model, all the channels do not make significant contributions to the formation of a given residual nucleus. For instance, for the formation of ^{197}Hg the first three channels only make significant contributions. For ^{198}Au, channel 1 contributes with almost unit probability. The variations of $\mathcal{P}_i(Z, A)$ with incident energy is shown in Fig. 5 for ^{198}Tl, ^{197}Hg, and ^{196}Au. For ^{198}Tl, channel 2, with a single PEQ neutron emission, is the most important channel between incident energies of 35 and 55 MeV. PEQ emission of two neutrons (channel 1) becomes stronger with increasing energy, but channel 2 continues to dominate in the energy region investigated. Channel 3, where all three neutrons undergo EQ emission, is important only at lower energies. For ^{197}Hg, also, channel 2 (PEQ proton emission) is the strongest channel, although channel 1 (simultaneous PEQ emission of a proton and a neutron) is also important for energies above 40 MeV. Channel 3 contributes very little to the formation of ^{197}Hg. For ^{196}Au, channel 3 (EQ alpha emission followed by EQ neutron emission) is the most important channel with PEQ
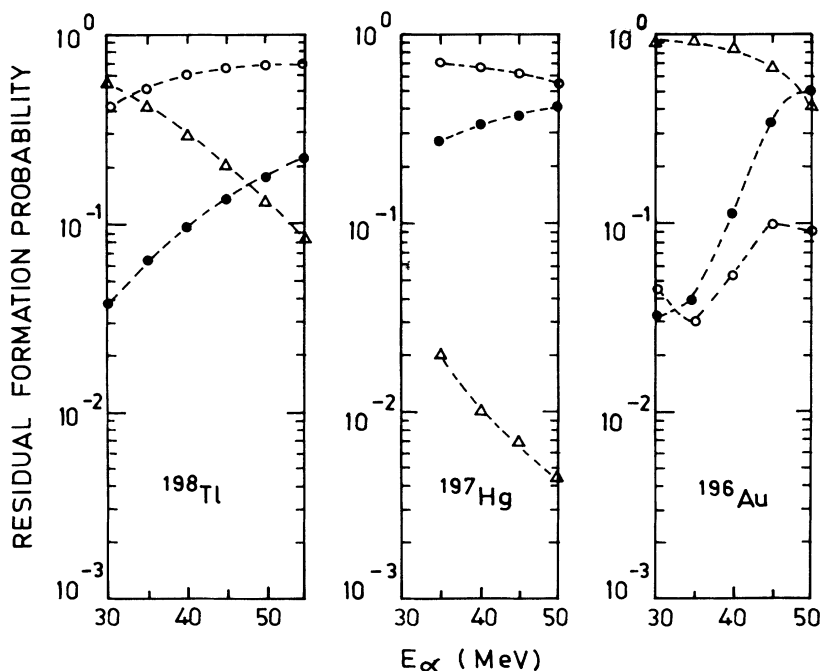

FIG. 5. Variation of the formation probability of the residual nuclei ^{198}Tl, ^{197}Hg, and ^{196}Au with respect to the incident alpha energy E_α for channels 1 (●), 2 (○), and 3 (△). The channels are defined in Table III. The lines are guides to the eye.

neutron emission (channel 1) becoming significant for energies above 45 MeV.

The comparison of the calculated IR's with experiment are shown in Figs. 1–4. For ^{198}Tl (Fig. 1) all four calculations with $\sigma^2 = \sigma_{II}$ assumptions (A), (B), (C), and (D) and calculations with $\sigma^2 = \sigma_I$ and assumptions (B), (C), and (D) show reasonable agreement with experimental IR's of Ref. [13]. The calculations are somewhat large compared with the values of Ref. [11] and the present measurements. The calculations with assumption (A) and σ_I overpredict the IR values. It is also to be noted that the effects of assumptions (B) and (C) to reduce the IR values with respect to assumption (A) are more pronounced for the larger value of $\sigma^2 = \sigma_I$.

For ^{197}Hg (Fig. 2) all the calculated IR values overpredict the observed IR values. The discrepancies are larger for the calculations with σ_I, particularly with assumption (A). Calculations with assumption (B) and σ_{II} are closest to the experimental values.

The calculations for ^{198}Au (Fig. 3) show the strong effect of assumptions (B) and (C). Use of σ_I and assumption (A) overpredict the IR values by an order of magnitude for $E_\alpha \cong 35$ MeV and by two orders of magnitude or more for higher values of E_α. The discrepancies are reduced, but are still too large for calculations with σ_{II} and assumption (A). With assumption (C) and σ_I, there is a drastic reduction in the IR values, but the overpredictions persist. Similar but less pronounced decreases in IR values are found with assumption (C) and σ_{II}. With assumption (B), however, the calculations underpredict the IR values for both σ_I and σ_{II}, and the IR values corresponding to assumption (D) come close to the experimental values, although the overpredictions persist, albeit on a lower scale, for the higher values of projectile energy.

For ^{196}Au (Fig. 4) the calculated values with σ_I are too large. Calculations with σ_{II} overpredict the experimental values of the present work for lower projectile energies, but are in good agreement with those of Ref. [7]. Also, since the effects of PEQ emissions are weak (only PEQ neutron emission is considered and PEQ alpha emission is neglected), there is little difference between the calculations of assumptions (A) and (C) with both σ_I and σ_{II}. Calculations with assumption (B) show a slight decrease in IR's for higher energies.

D. Sensitivity of isomer ratios to model parameters

As can be seen in Figs. 1–4, the calculated IR's in general overpredict the experimental values and the overprediction is more for calculations with $\sigma^2 = \sigma_I$. The discrepancy is most serious for ^{196}Au and ^{197}Hg and less so for ^{198}Au. For ^{198}Tl the calculations agree well with one set of experiments [13], which again are a little higher than the values of Ref. [11] and the present work. The principal reason for the overprediction is the use of the assumption of sharp branching of gammas to the metastable and ground states. All the states with spin larger than the metastable state spin will not decay exclusively to the isomeric state as has been assumed. Some of them may decay to the ground state and thereby decrease the IR's.

Qaim, Mushtaq, and Uhl [4] have shown a comparison of calculations of IR $= \sigma_m / (\sigma_m + \sigma_g)$ performed with the sharp branching assumption and actual multipole gamma transitions for a ^{70}Ge$(\alpha, n)^{72}$Se reaction. The two results differ approximately by a factor of 2 over the entire incident energy range of 13–27 MeV, although the trend remains the same. The difference will be somewhat larger for IR $= \sigma_m / \sigma_g$. Also, in their calculations the sharp branching assumption underpredicts $\sigma_m / (\sigma_m + \sigma_g)$ because the metastable-state spin is less than the ground-state spin. When the ground-state spin is lower, the sharp branching assumption will overpredict the IR values as in our case.

For ^{196}Au, apart from the sharp branching assumption, an important cause for the overprediction is the neglect of PEQ alpha emission. This is expected to occur with a large probability. This will not only alter the values of $\mathcal{P}_i(Z, A)$, but on account of the large angular momentum carried by the PEQ alpha, there will be substantial depletion of the higher spin states of ^{196}Au resulting in lower values of IR's.

It can also be seen from Figs. 1–4 that the IR calculated with $\sigma^2 = \sigma_I$ is always more than that obtained with $\sigma^2 = \sigma_{II}$. The spin distribution following EQ emission [or PEQ emission with assumption (A)] depends sensitively on σ^2. The larger the values of σ^2, the greater will be the population of the higher spin states and the larger the calculated IR values. It is a common practice to use a value of σ^2 corresponding either to the rigid-body moment of inertia or a fraction (usually half) of it. Qaim, Mushtaq, and Uhl [4], Bissem et al. [9], and Marten et al. [10] have found better fits with their measured IR's using σ^2 corresponding to half the rigid-body moment of inertia. The IR's investigated in Refs. [4], [9], and [10] are those of nuclei formed through neutron emissions. Nagame et al. [7], who investigated the IR's of nuclei formed through neutron as well as charged-particle emissions, find that the full rigid-body moment of inertia gives better agreement with the IR's of ^{196}Tl and ^{198}Tl produced through ^{197}Au$(^3$He, $4n)$ and ^{197}Au$(\alpha, 3n)$ reactions, respectively. It should, however, be noted that their experimental values of the IR's for ^{198}Tl are much larger than the measurements of other authors [11,13] and the present work, as can be seen in Fig. 1. It is also seen from Fig. 1 that calculations with $\sigma^2 = \sigma_I$ (half rigid-body moment of inertia) as well as with lower value of $\sigma^2 = \sigma_{II}$ give satisfactory agreement with the results of Ref. [13]. The inclusion of appropriate gamma branching to metastable and ground states will bring our calculated IR's closer to those of Ref. [11] and the present work.

A different behavior is observed for charged-particle emissions. The calculations of Nagame et al. [7] with multipole gamma transitions taken into account and σ^2 obtained from full rigid-body moment of inertia overpredict the IR values of ^{197}Au$(^3$He, $2p)^{198}$Au by three orders of magnitude and for ^{197}Au$(^3$He, $\alpha)^{196}$Au as well as ^{197}Au$(\alpha, \alpha'n)^{196}$Au reactions by one order of magnitude. For the last reaction, Fig. 4 shows the effect of using a lower value of σ^2. Calculations with $\sigma^2 = \sigma_{II}$ do bring down the IR values close to the measured values of

Nagame *et al.* compared with the calculated values with $\sigma^2 = \sigma_{\rm I}$. However, the overpredictions in the calculations of Nagame *et al.* do not arise from the larger values of σ^2 alone. These authors do not take into account the depletion in the population of the higher spin states by PEQ emissions. They assume the spin distribution after PEQ emission to be the same as that of the target and projectile system. In our calculations also the PEQ effects have not been considered fully for the ^{197}Au$(\alpha,\alpha'n)$ ^{196}Au reaction as PEQ alpha emission is expected to occur for the incident energies investigated. This would reduce the calculated IR values, as discussed earlier, and bring them closer to the present measured values. From the present calculations of IR's for ^{197}Hg, ^{198}Au, and ^{196}Au formed through charged-particle emissions, it seems that a lower value of $\sigma^2 \sim \sigma_{\rm II}$ together with proper branching of multipole gammas to the metastable and ground states is expected to give better agreement with experiment.

The strong effect of PEQ emissions, particularly of charged ejectiles, on the spin distribution can be seen from a comparison of the experimental IR's for ^{198}Tl, ^{197}Hg, and ^{198}Au in the incident energy range of 35–50 MeV. Compared with the IR's for ^{198}Tl, the IR's for ^{197}Hg are less by a factor of 5–10 on the average, while those of ^{198}Au are almost two orders of magnitude less. The spin difference $\Delta J = J_m - J_g$ between the spin J_m of the metastable state and J_g of the ground state is $5\hbar$ for ^{198}Tl, $6\hbar$ for ^{197}Hg, and $10\hbar$ for ^{198}Au (Table II). The larger value of ΔJ for ^{198}Au may be one reason for the

low IR values of this nucleus. On the other hand, the difference between ΔJ of ^{198}Tl and ^{197}Hg is not large enough to explain the significantly lower values of IR's for ^{197}Hg compared with ^{198}Tl. The difference between the spin distributions of ^{197}Hg and ^{198}Tl on account of the extra proton for the formation of ^{197}Hg may be responsible for the lower population of the metastable state of ^{197}Hg. The proton, unlike the neutron, has to overcome the Coulomb barrier at the time of emission. The proton spectrum, therefore, has fewer low-energy particles than the neutron spectrum. For the same impact parameter, the proton carries away more angular momentum than the neutron because the proton energy spectrum is shifted more toward higher energies.

Figure 6 shows a comparison of the spin distributions of the residual nuclei ^{198}Tl, ^{198}Au, and the intermediate nucleus ^{198}Hg [formed in the course of a ^{197}Au$(\alpha,3pn)^{197}$Hg reaction] at 35 MeV incident energy with $\sigma^2 = \sigma_{\rm II}$. The calculations are for channel 1 (see Table III), where the reactions start with the simultaneous PEQ emission of two nucleons—two neutrons for ^{198}Tl, a proton and a neutron for ^{198}Hg, and two protons for ^{198}Au—followed by EQ neutron emission. The reason for choosing channel 1 is that ^{198}Au is formed almost entirely through this channel, and ^{197}Hg has also a strong probability of formation through channel 1. Though channel 1 contributes weakly to the formation of ^{198}Tl, the maximum depletion of population of higher spin states of ^{198}Tl takes place when the $(\alpha,3n)$ reaction
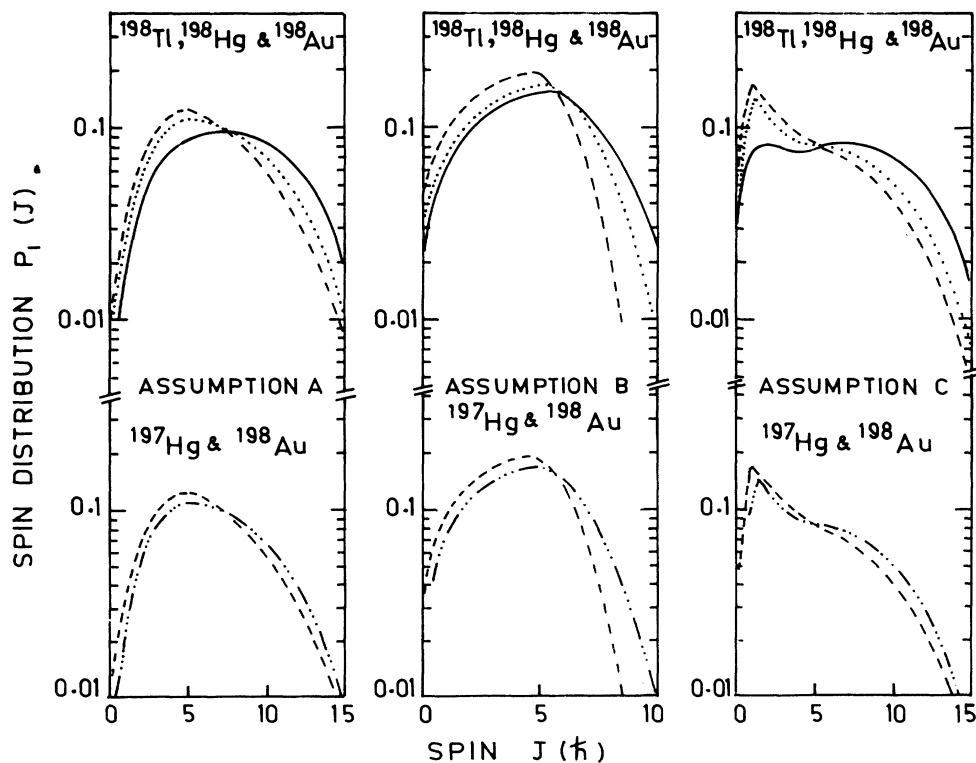

FIG. 6. Comparison of the spin distributions of ^{198}Tl (———), ^{198}Hg (· · · ·), and ^{198}Au (— — —) (upper part) and ^{197}Hg (– · · · –) and ^{198}Au (lower part) formed through channel 1 (Table III) at incident energy of 35 MeV for assumptions (A), (B), and (C) of PEQ angular distribution with $\sigma^2 = \sigma_{\rm II}$.

proceeds through this channel. All three nuclei ^{198}Tl, ^{198}Hg, and ^{198}Au are formed through the emission of three ejectiles, but the proton multiplicity varies form 0 to 2. As can be seen, the population of the higher spin states decreases with increasing proton multiplicity.

Figure 6 also shows the comparison of the spin distributions of ^{197}Hg with ^{198}Au. The EQ emission of the fourth ejectile, a neutron, from ^{198}Hg causes further depletion of the higher spin states of ^{197}Hg compared with ^{198}Hg. It can be seen that even with the extra neutron emission the population of higher spin states of ^{197}Hg is less depleted than those of ^{198}Au. This shows that more angular momentum is lost in the emissions of two protons and one neutron than in the emission of one proton and three neutrons. The higher spin population depletion is most pronounced for assumption (B) and less so but still significant for assumptions (A) and (C).

The effect of the three assumptions (A), (B), and (C) of PEQ angular distribution on the residual nucleus spin is shown in Figs. 7 and 8. Figure 7 shows the calculated spin distributions with $\sigma^2 = \sigma_{II}$ for the first intermediate nucleus ^{200}Tl and the final nucleus ^{198}Tl formed through the ^{197}Au($\alpha, 3n$)^{198}Tl reaction at 35 MeV incident energy. Calculations for channels 2 and 3 only are shown since ^{198}Tl is formed predominantly through these two channels, as can be seen in Fig. 5. In channel 2 a PEQ neutron emission is followed by EQ emission of two neutrons, and in channel 3 all three neutrons undergo EQ emission. For channel 2 the spin distributions for all the three assumptions are shown. In channel 3 (EQ emissions only), only assumption (A) is valid. The maximum depletion in the population of higher spin states is

achieved when the PEQ emission is assumed to take place in the incident direction in a single-step interaction between the projectile and target nucleus [assumption (B)]. Assumption (C) which, like (B), assumes total alignment of incoming and outgoing orbital angular momentum, but, unlike (B), takes into account PEQ emissions from every stage of the intranuclear cascade, gives far less depletion of the higher spin states than (B). The least angular momentum is carried away by EQ emission (channel 3); even with fully isotropic angular distribution (A), a PEQ ejectile carries away more angular momentum because of its higher energy.

A comparison of the spin distributions resulting from two- and single-nucleon PEQ emissions is shown in Fig. 8 for the ^{197}Au($\alpha, p3n$) ^{197}Hg reaction at 50 MeV, where channel 1 (two-nucleon PEQ emission) and channel 2 (single-nucleon PEQ emission) contribute with comparable strengths (Fig. 5). The figure shows the variation of the cumulative probability $P_S(J_N)$, with spin J_N for $\sigma^2 = \sigma_{II}$. The cumulative probability is the sum of the probabilities of occupation of all states with spin greater than J_N, i.e., $P_S(J_N) = \sum \overline{P(J_i)}$ for all $J_i \geq J_n$, with $\overline{P(J_i)}$ obtained from (23). For the lowest J_N, $P_S(J_N) = 1$ and the value of $P_S(J_N)$ for a given J_N is a measure of the population of states with spins greater than and equal to J_N. That two PEQ nucleons carry away much larger angular momentum than a single PEQ nucleon is evident from the strong depletion of higher-spin-state occupancies in channel-1 calculations with assumption (B) compared with channel-2 calculations. In general, for all three assumptions (A), (B), and (C), more angular momentum is carried away through two PEQ emissions.
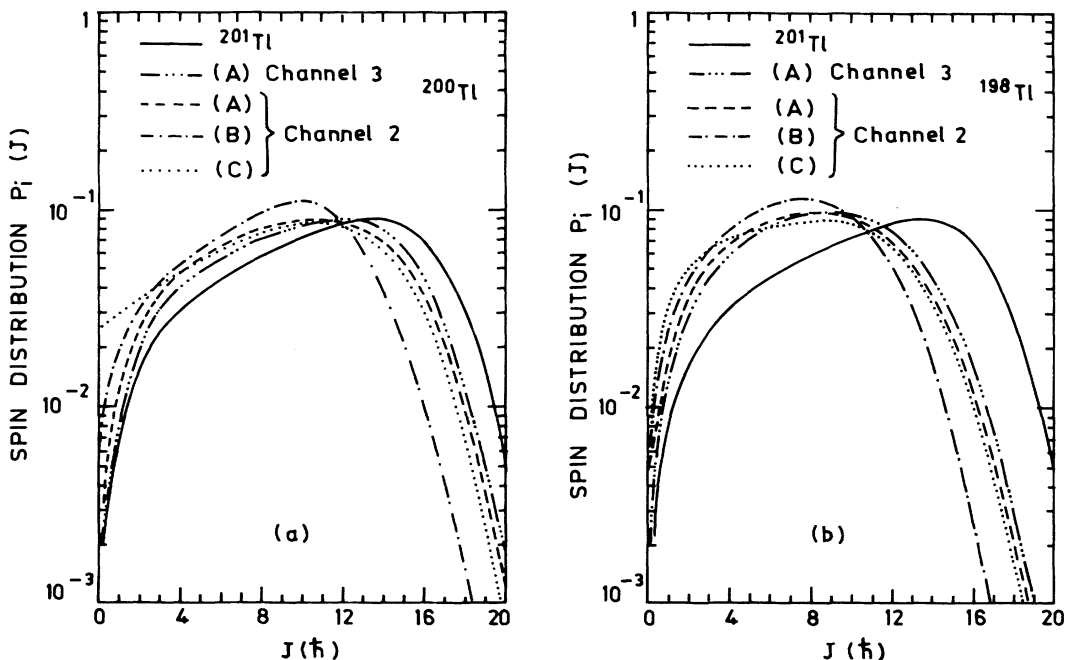

FIG. 7. The spin distributions of (a) ^{200}Tl and (b) ^{198}Tl formed through channel 3 with assumption (A) (– $\cdots$ –) and channel 2 with assumptions (A) (– – –), (B) (– $\cdot$ –), and (C) ($\cdots$). The spin distribution of the target and projectile ^{201}Tl is also shown (———) for comparison. The incident energy is 35 MeV and $\sigma^2 = \sigma_{II}$.

It should be noted that for both ^{198}Tl (Fig. 7) and ^{197}Hg (Fig. 8) the change in the spin distributions between (C) and (A) is not very large, although the population of higher spin states is less with assumption (C). Far more angular momentum is lost through PEQ emission when assumption (B) is used. This shows that alignment of incoming and outgoing orbital angular momenta is not the only factor responsible for depletion of higher-spin-state population. The number of two-body interactions prior to PEQ emission is also important in determining the angular momentum lost through emission. Each two-body interaction changes the impact parameter of the ejectile, but PEQ emissions may not take place with equal probability, as has been assumed, from all possible values of impact parameters from zero to the nuclear radius. If the bulk of PEQ emissions occurs after only a few two-body interactions, then the ejectile impact parameters will be clustered around the incident impact parameter. If only these impact parameters are considered in (C), then the population of higher spin states will be considerably lower. The present calculations with assumption (C) give the upper bound and those with (B) the lower bound of the occupation of the higher spin states after PEQ emissions. The IR's calculated with assumption (D), the weighted average of (B) and (C), will be lower for both ^{198}Tl and ^{197}Hg if proper distribution of impact parame-
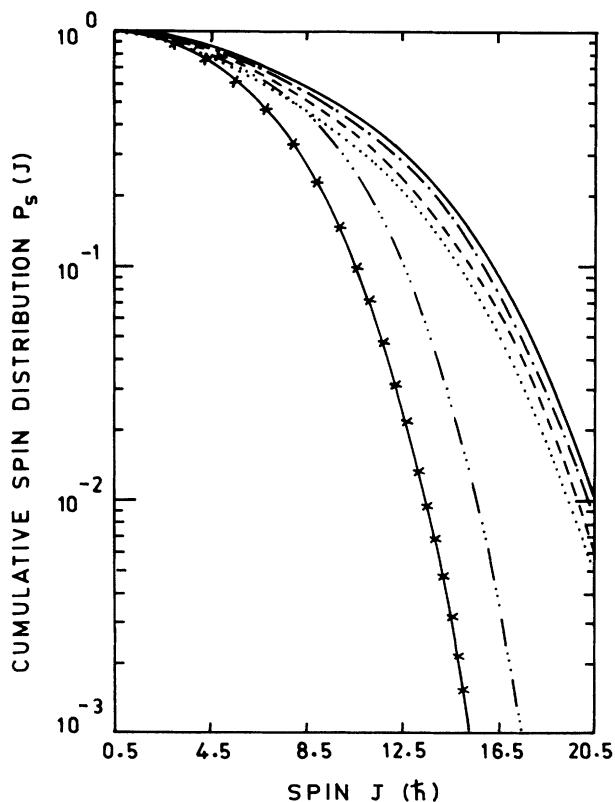

FIG. 8. Variation of the cumulative spin distribution $P_s(J)$ (see text) of ^{197}Hg with spin J at incident energy of 50 MeV with $\sigma^2 = \sigma_{II}$. Calculations are for channel 1 with assumptions (A) (– – –), (B) (– ✕ –), and (C) (· · ·) and for channel 2 with assumptions (A) (———), (B) (– · · · –), and (C) (– · –).

ters is considered. For ^{198}Au this correction in (C) will drastically reduce the IR values calculated with (D) because of the large difference in the IR's obtained by (B) and (C), as shown in Fig. 3.

The importance of multiple PEQ emissions can be seen from the calculated IR's for ^{198}Au. In the present calculations, ^{198}Au is formed with almost unit probability through the simultaneous PEQ emission of two protons followed by EQ neutron emission (channel 1 of Table III). If the PEQ emission is restricted to a single proton (channel 2, Table III), then, as shown in Fig. 9, the angular momentum lost is much less with corresponding increase in IR values resulting in larger discrepancy between calculation and observation.

VI. SUMMARY AND CONCLUSIONS

Excitation functions of IR's for ^{198}Tl, ^{197}Hg, ^{198}Au, and ^{196}Au formed through $\alpha + ^{197}$Au reactions have been measured in the incident energy range of 35–50 MeV. The IR's for ^{197}Hg and ^{198}Au are reported for the first time. The IR's for ^{196}Au have been reported earlier [7] for $E_\alpha \leq 40$ MeV. The measured IR's for ^{198}Tl are in good agreement with the previous measurements fo Refs. [11] and [13], but are far less than the values of Ref. [7]. Similarly, the IR's for ^{196}Au as measured by Ref. [7] are in excess of the present measurements in the region of overlapping incident energies.

The disagreements between the present and earlier measurements of the cross sections of some of the isomers have been examined in terms of more recent decay scheme data. Some of the discrepancies are removed thereby. Other possible reasons for the disagreements have been discussed. The disagreements in the cross sectons of ^{198}Tl^g and ^{196}Au^m between the present measurements and those of Ref. [7] could not be explained.

The observed IR's have been analyzed in terms of both PEQ and EQ emissions. Multiple PEQ emissions have been taken into account. PEQ emissions, however, have been restricted to nucleons only. The different sequence of ejectiles and their different emission mechanisms (PEQ and EQ) have been explicitly considered to obtain the average spin distribution of the residual nucleus.

It is to be noted that when the observed excitation function of $\sigma_m + \sigma_g$ has been fairly well reproduced, as in the case of ^{198}Tl, the calculated IR's show reasonable agreement with experiment. On the other hand, for ^{197}Hg, ^{198}Au, and ^{196}Au, the calculated excitation functions as well as the IR's disagree with experiment.

The excitation function calculations are dependent on the choice of the level-density parameters, as also on the reaction mechanisms considered. The level-density parameter strongly influences EQ emission cross sections, but this has little effect on the spin distribution. The IR's calculated with a different level-density parameter ($C = 9$) did not show any significant change from the values presented in this work. An inadequate description of the reaction mechanism is the more likely cause for the disagreement between observed and calculated values of excitation functions and IR's. For instance, in the model calculations for ^{197}Hg, ^{198}Au, and ^{196}Au, only nucleon
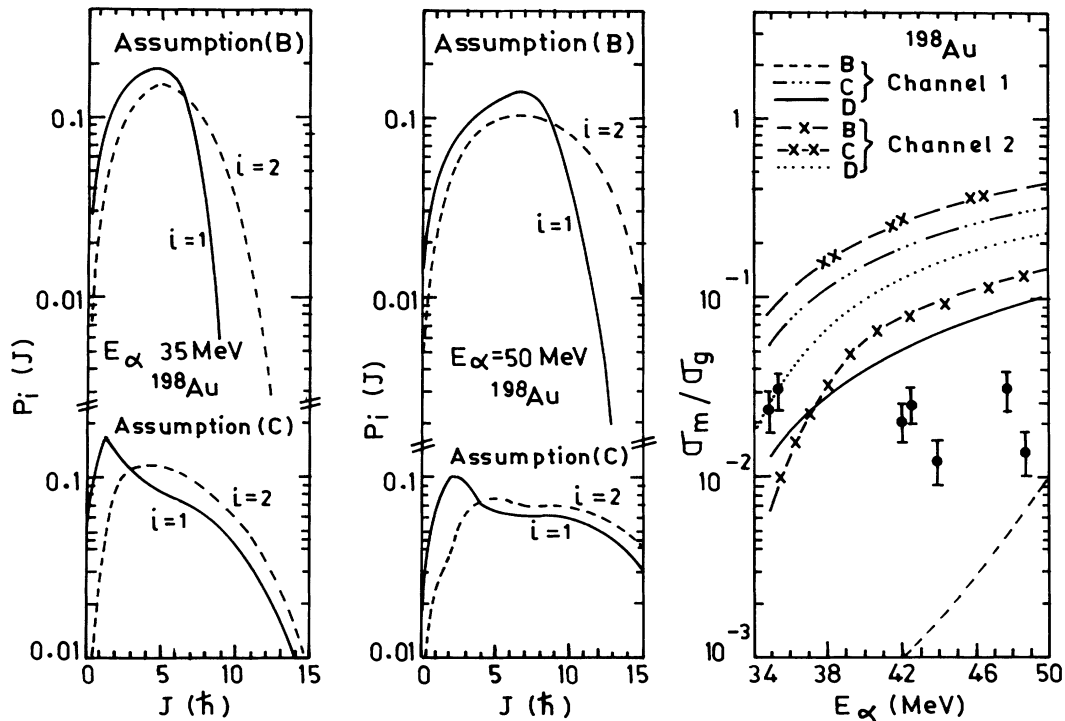
FIG. 9. Comparison between the spin distributions of ^{198}Au formed exclusively through either channel $i = 1$ or 2 (Table III) under assumptions (B) and (C) for incident energies 35 and 50 MeV with $\sigma^2 = \sigma_{II}$. The corresponding σ_m/σ_g are compared with experiment in the figure on the extreme right.

emissions are considered in the PEQ channels. PEQ cluster emissions which affect both the formation cross sections and spin distribution of residual nuclei have been neglected in the hybrid model calculations. In spite of this inadequacy in the treatment of the reaction mechanism and the assumption of sharp branching of gammas to metastable and ground states, the results of the model calculations give a qualitative description of how different parameters influence the spin distribution and IR's.

PEQ protons carry away more angular momentum than PEQ neutrons, and for proton emissions PEQ emission is the dominant reaction mechanism. Also, for more than one proton emission, multiple PEQ emissions play

an important role in the reaction process.

Spin distributions resulting from PEQ emissions are strongly sensitive to the PEQ angular distribution. For EQ emissions the spin cutoff parameter determines the spin distribution. For nuclei formed through PEQ emissions followed by EQ emission, a proper evaluation of the spin cutoff parameter can be arrived at only after considering multiple PEQ emissions including that of clusters with proper angular distribution. This is more important for charged-particle emissions where the customary use of spin cutoff parameter obtained from the full rigid-body moment of inertia or half its value results in gross overprediction of IR values.

[1] J. R. Huizenga and R. Vandenbosch, Phys. Rev. 120, 1305 (1960).

[2] R. Vandenbosch and J. R. Huizenga, Phys. Rev. 120, 1313 (1960).

[3] C. T. Bishop, J. R. Huizenga, and J. P. Hummel, Phys. Rev. 135, B401 (1964); H. Groening, K. Aleklett, K. J. Moody, P. L. Macgaughey, W. Loveland, and G. T. Seaborg, Nucl. Phys. A389, 80 (1982); K. J. Moody and J. J. Hogan, Phys. Rev. C 34, 899 (1986); E. A. Skakum, V. S. Batil, Yu. N. Rakivnenko, and O. A. Rastrepin, Yad. Fiz. 46, 28 (1987) [Sov. J. Nucl. Phys. 46, 17 (1987)].

[4] S. M. Qaim, A. Mushtaq, and M. Uhl, Phys. Rev. C 38, 645 (1988).

[5] S. Fukushima, S. Kume, H. Okamura, K. Otozai, K. Sakamoto, Y. Yoshizawa, and S. Hayashi, Nucl. Phys. 69, 273 (1965); P. Misaelides and H. Munzel, J. Inorg. Nucl.

Chem. 42, 937 (1980); L. T. Auler, A. G. de Silva, and G. W. A. Newton, ibid. 43, 2611 (1981); G. W. A. Newton, V. J. Robinson, and E. M. Shaw, ibid. 43, 2227 (1981).

[6] I. S. Grant and M. Rathle, J. Phys. G 5, 1741 (1979).

[7] Y. Nagame, K. Sueki, S. Baba, and H. Nakahara, Phys. Rev. C 41, 889 (1990).

[8] J.-P. Didelez, R. M. Lieder, H. Beauscher, D. R. Haenni, H. Machner, M. Müller-Veggian, and C. Mayer-Böericke, Nucl. Phys. A341, 421 (1980); H. I. West, Jr., R. G. Lanier, and M. G. Mustafa, Phys. Rev. C 35, 2067 (1987).

[9] H. H. Bissem, R. Georgi, W. Scobel, J. Ernst, M. Kaba, J. Rama Rao, and H. Strohe, Phys. Rev. C 22, 1468 (1980).

[10] M. Marten, A. Schuring, W. Scobel, and H. J. Probst, Z. Phys. A 322, 93 (1985).

[11] F. M. Lanzafame and M. Blann, Nucl. Phys. A142, 545 (1970).

[12] H. E. Kurz, E. W. Jasper, K. Fisher, and E. Hermes, Nucl. Phys. A168, 129 (1971).

[13] O. A. P. Capurro, M. de la Vega Vedoya, C. Wasilevsky, and S. J. Nassif, J. Radioanal. Nucl. Chem. 89, 519 (1985).

[14] M. Blann, Lawrence Livermore National Laboratory Report No. UCID 19614, 1982.

[15] M. Blann, Phys. Rev. Lett. 27, 337 (1971).

[16] M. Blann, Phys. Rev. Lett. 28, 757 (1972).

[17] M. Blann and V. K. Vonach, Phys. Rev. C 28, 1475 (1983).

[18] V. F. Weisskopf and D. H. Ewing, Phys. Rev. 57, 472 (1940).

[19] C. F. Williamson, J. P. Boujot, and J. Picard, Centre d'Etude Nucléaires de Saclay Report No. CEA-R-3042, 1966.

[20] U. Martens and G. W. Schweimer, Kernforschungszentrum, Karlsruhe, Report No. KFK-1083, 1969.

[21] J. J. Routi and S. G. Prussoin, Nucl. Instrum. Methods 72, 145 (1969).

[22] S. S. Rattan, Bhabha Atomic Research Centre, Bombay, India, Report No. BARC-1527, 1990.

[23] U. Reus and W. Westmeier, At. Data Nucl. Data Tables 29, 1 (1983).

[24] P. K. Sarkar, T. Bandyopadhyay, G. Muthukrishnan, and S. Ghosh, Phys. Rev. C 43, 1855 (1991).

[25] C. Kalbach and F. M. Mann, Phys. Rev. C 23, 112 (1981).

[26] G. Mantzouranis, H. A. Weidenmüller, and D. Agassi, Z. Phys. A 276, 145 (1976); N. C. Chiang and J. Hüfner, Nucl. Phys. A349, 466 (1980); M. Blann, W. Scobel, and H. Plechaty, Phys. Rev. C 30, 1493 (1984).

[27] A. De, S. Ray, and S. K. Ghosh, Phys. Rev. C 37, 2441 (1988).

[28] J. H. E. Mattauch, W. Thiele, and A. H. Wapstra, Nucl. Phys. 67, 1 (1965).

[29] W. D. Myers and W. J. Swiatecki, Ark. Fys. 36, 343 (1969).

[30] J. R. Huizenga and G. J. Igo, Nucl. Phys. 29, 462 (1962).

[31] M. Blann, Annu. Rev. Nucl. Sci. 25, 123 (1975); R. Michel, F. Peiffer, and R. Stuck, Nucl. Phys. A441, 617 (1985).

[32] A. Djaloesis, P. Jahn, H. J. Probst, and C. Mayer-Böericke, Nucl. Phys. A250, 149 (1975); M. Blann and T. T. Komoto, Phys. Rev. C 39, 1678 (1983).

[33] R. Michel and G. Brinkmann, Nucl. Phys. A338, 167 (1980).